

Journal of Biomedical Optics

BiomedicalOptics.SPIEDigitalLibrary.org

Mapping optical path length and image enhancement using quantitative orientation-independent differential interference contrast microscopy

Michael Shribak
Kieran G. Larkin
David Biggs

SPIE.

Michael Shribak, Kieran G. Larkin, David Biggs, "Mapping optical path length and image enhancement using quantitative orientation-independent differential interference contrast microscopy," *J. Biomed. Opt.* **22**(1), 016006 (2017), doi: 10.1117/1.JBO.22.1.016006.

Mapping optical path length and image enhancement using quantitative orientation-independent differential interference contrast microscopy

Michael Shribak,^{a,*} Kieran G. Larkin,^b and David Biggs^c

^aMarine Biological Laboratory, 7 MBL Street, Woods Hole, Massachusetts 02543, Unites States

^bNontrivialzeros Research, 22 Mitchell Street, Putney, New South Wales 2112, Australia

^cKB Imaging Solutions, 3849 Val Verde Road, Loomis, California 95650, Unites States

Abstract. We describe the principles of using orientation-independent differential interference contrast (OI-DIC) microscopy for mapping optical path length (OPL). Computation of the scalar two-dimensional OPL map is based on an experimentally received map of the OPL gradient vector field. Two methods of contrast enhancement for the OPL image, which reveal hardly visible structures and organelles, are presented. The results obtained can be used for reconstruction of a volume image. We have confirmed that a standard research grade light microscope equipped with the OI-DIC and 100 \times /1.3 NA objective lens, which was not specially selected for minimum wavefront and polarization aberrations, provides OPL noise level of ~ 0.5 nm and lateral resolution if ~ 300 nm at a wavelength of 546 nm. The new technology is the next step in the development of the DIC microscopy. It can replace standard DIC prisms on existing commercial microscope systems without modification. This will allow biological researchers that already have microscopy setups to expand the performance of their systems. © 2017 Society of Photo-Optical Instrumentation Engineers (SPIE) [DOI: [10.1117/1.JBO.22.1.016006](https://doi.org/10.1117/1.JBO.22.1.016006)]

Keywords: differential interference contrast microscopy; interference microscopy; microscopy; phase retrieval; interferometric imaging.

Paper 160660R received Sep. 24, 2016; accepted for publication Dec. 12, 2016; published online Jan. 6, 2017.

1 Introduction

A differential interference contrast (DIC) microscope is a powerful and commonly used tool for biological research. The DIC image is produced by interference of the light field coming from the object with a laterally displaced copy of itself.¹⁻⁶ The DIC microscope can employ a high numerical aperture (NA) objective and condenser lenses and, therefore, provides good lateral resolution as well as good axial discrimination. The shear distance is usually smaller than the Airy disk radius,⁷ and it does not affect the lateral resolution substantially. Very weak features can be seen with good contrast because the image intensity is a sine squared function⁸ of the specimen's phase gradient in the direction of the shear. However information in the direction perpendicular to the shear is lost. It is, therefore, prudent to examine unknown objects at several azimuth orientations.^{4,5}

Digital processing of several DIC images taken at the orthogonal shear-directions facilitates the retrieval of the quantitative phase image or optical path length (OPL) map. Preza⁹ proposed an iterative phase-estimation method for the calculation of a specimen's phase map, which starts from a guess phase image. She used two, four, or eight regular DIC images with the same bias $\sim \pi/2$, but with shear directions differing by 90 deg, 45 deg, or 22.5 deg, respectively. Preza's results showed that the major significant improvement in the phase image is achieved when two orthogonal DIC images (with a 90-deg shear angle separation) are used. Using DIC images with more than two shear directions does not provide substantial improvement.

Preza did not use DIC images with a pair of biases with same magnitude amount and opposite signs because it was supposed that they could be useful in reduction of noise only. The iterative phase-estimation method assumes an object with no absorption. Recently, Preza and O'Sullivan developed an alternating minimization method that extends the iterative phase-estimation approach and can be used to estimate object amplitude.¹⁰

Arnison et al.¹¹ described using the spiral phase integration to produce a phase image from two sets of conventional DIC images at the orthogonal shear directions. Each set consists of four images with the biases 0, $\pi/2$, π , and $3\pi/2$, which are used to compute corresponding orthogonal phase gradient components.¹² The gradient computation removes both the object absorption and vignetting from the signal and obtains phase gradients in the orthogonal directions. It also removes phase-independent system errors, such as weak spots on the camera or nonuniform illumination. Then the phase image is obtained by Fourier integration of the phase gradient data. Because the shear distance is unknown, the computed image is only linearly proportional to the true phase and requires further calibration.

King et al.¹³ described a calibration technique to find the corresponding proportionality factor in the spiral phase integration. The authors employ a linear regression analysis of experimental images of a 2- μ m polystyrene bead. In another publication, King et al.¹⁴ used a preliminary known shear distance and provided a more detailed description of the spiral phase integration. They also proposed a technique for the alignment of images after mechanically rotating the specimen.

*Address all correspondence to: Michael Shribak, E-mail: mshribak@gmail.com

The aforementioned techniques rely on mechanical rotation of the specimen, which raises two serious practical issues. The first issue is maintaining focus while rotating the specimen. The second issue is the error due to misaligned images, which causes artifacts in the processed images. In addition, the mechanical manipulations usually take about 10 s. This introduces a time delay between images. In the case of studying a living specimen, the delay creates an additional significant problem due to the dynamic nature of the sample.

Kou and Sheppard¹⁵ reported a phase restoration technique that combines phase-shifting DIC and phase microscopy based on the transport-of-intensity equation. Their technique does not require rotation of the specimen. At first, the authors obtained phase gradient information in one direction using four images as described by Cogswell et al.¹² Then the image is defocused in the both directions, and two more image sets are captured. Thus, 12 raw images have to be captured in total. The phase image is computed using an inverse Laplacian method. However, the images produced are quite blurred. Kou and Sheppard also indicated that the spiral phase integration turns out to be the same as an inverse Laplacian method used in early three-dimensional (3-D) computer vision attempts to obtain the shape of the object from shading.¹⁶

McIntyre et al.^{17,18} introduced DIC microscopy using a spatial light modulator (SLM) that is placed in the back focal plane of the objective. The SLM acts as a diffractive optical element, which is computer controlled, allowing selection of beam shear distance, beam shear direction, and bias. The authors have also demonstrated that a set of nine DIC images with the orthogonal shear directions can be obtained in a single shot using this approach, but it would require a more complex SLM mask. The set consists of two pairs of three DIC images with the bias step $2\pi/3$ and three dummy images. The SLM-DIC microscope uses a laser as the light source. Unlike a conventional interferometric scheme, the setup does not split the illumination beam and then recombine the interfering beams. The SLM-DIC microscope employs a rotating diffuser, which removes the effective temporal coherence of the laser beam by time averaging and reduces the contrast of the disturbing speckle pattern. The partial spatial coherence of the interfering beams is obtained by restriction of the condenser lens NA to 0.38, while the objective lens NA is 1.3. The degree of spatial coherence also depends on the shear distance. Because two interfering beams are not completely mutually coherent, the image contrast is reduced. The best reported image contrast was about 50%.¹⁸ The microscope has limited sectioning capability. High-resolution objective lenses have a very small Airy disk and require the use of a correspondingly small shear distance. However, it is not possible to make the shear distance arbitrarily small with an SLM because of the finite pitch of the pixels. The reported minimum shear distance is 130 nm.¹⁸ This is double the shear of a standard high-resolution Olympus Nomarski DIC prism U-DICTH.⁶ In addition, the microscope suffers from light energy loss. It only uses the first diffraction orders. The other diffraction orders are eliminated by a beam dump¹⁷ or slit.¹⁸ The slit also reduces the field of view.

Zahreddine et al.¹⁹ described a DIC microscope that employs two pairs of orthogonal liquid crystal (LC) prisms instead of two standard DIC prisms. The beam shear distance introduced by the LC prism depends on the applied voltage. The setup also includes a standard phase-shifting LC cell in order to control the bias. The authors stated “the LC prisms can be adjusted

to fit wherever is most convenient for the user.” We think this statement is not correct. In order to obtain the best contrast, the LC DIC prism assemblies have to be placed in the front and back focal planes of the condenser and objective, respectively. The working principle of the device was confirmed by the imaging of human cheek cells with a 20× objective lens.

The major problem of the aforementioned approaches using SLM or LC prisms is that they do not reproduce a beam tracing in the Nomarski DIC prism. The Nomarski prism separates the Poynting vector, which represents the energy flow direction and the wave normal. Therefore, a plane of localization of interference fringes⁵ (called also a plane of apparent splitting)²⁰ is located outside at some distance from the Nomarski prism. Their interference fringes are localized inside of the SLM or the LC prism, where the actual splitting occurs. In order to obtain a DIC image, the plane of interference fringe localization has to be superimposed with the objective back focal plane. Hence, the proposed SLM and LC prisms can only be used effectively with low-power microscope objectives whose back focal plane is localized outside their lens system. By contrast, the back focal plane of middle-power and high-power objectives is inside their optical system and cannot be brought into coincidence with the plane of localization of interference fringes of a typical Wollaston prism. To overcome this difficulty, Nomarski invented a birefringent prism whose interference fringes are localized outside it.³⁻⁵ It is also possible to employ an additional telescope in order to reimage the back focal plane of middle-power and high-power objectives.¹⁸

Shribak proposed the beam-shearing DIC assembly with external localization of interference fringes.^{8,21,22} The DIC assembly is computer controlled, allowing rapid selection of beam shear direction and bias. It can easily replace standard DIC prisms in existing commercial microscope systems without modification. This will allow biological researchers that already have microscopy setups to easily expand the performance of their systems.

2 Optical Set-Up of the Orientation-Independent DIC Microscope

In this section, a brief review of our previously published works about the quantitative orientation-independent differential interference contrast (OI-DIC) microscopy^{6-8,21-23} with updates is presented for completeness. The optical scheme of the OI-DIC assembly, which allows changing the shear direction, is shown in Fig. 1. It consists of two identical standard DIC prisms and a polarization rotator sandwiched between the prisms. The shear directions of the DIC prisms are orthogonal. We can assume that the first prism has a shear direction at 0 deg and

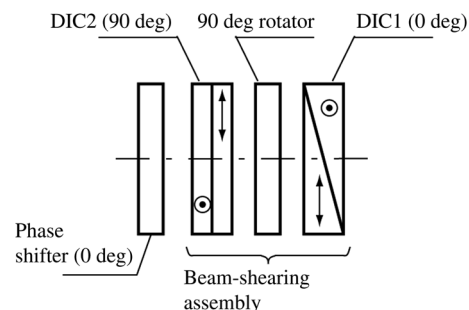


Fig. 1 Optical scheme of OI-DIC beam shearing assembly with phase shifter.


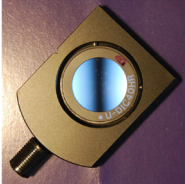
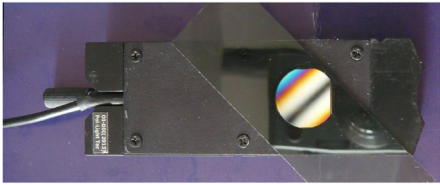
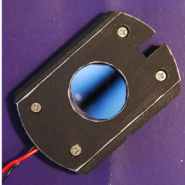
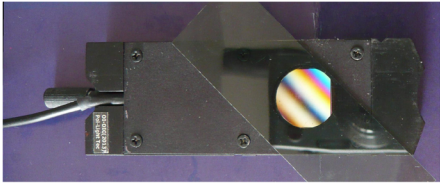
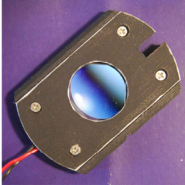
Shear directions	Objective-side sliders (imaging beam)	Condenser-side sliders (illuminating beam)
0 deg Olympus DIC prisms	 U-DICTHR	 U-DIC40HR
-45 deg OI-DIC assemblies, (OFF)	 OI-DIC-A	 OI-DIC-B
45 deg OI-DIC assemblies, (ON)	 OI-DIC-A	 OI-DIC-B

Fig. 2 Standard Olympus DIC sliders and new sliders with OI-DIC beam shearing assemblies in white light between crossed polarizers. Shear direction is perpendicular to the interference fringes.

the second prism has a shear direction at 90 deg. The polarization rotator works as a bistable element that rotates the beam polarization by 0 deg or 90 deg, called state OFF and state ON, accordingly. In particular, we employed a twisted-nematic (TN) LC cell as the 90-deg polarization rotator. In operation, the assembly shear direction can be oriented either at -45 deg or at 45 deg. The combined shear distance between the two interfering beams created by the OI-DIC assembly equals the shear distance of a single DIC prism multiplied by $\sqrt{2}$.

In order to vary the bias between the two interfering beams, the OI-DIC microscope includes a phase shifter. The phase shifter is an untwisted nematic LC cell, which works in the electrically controlled birefringence mode. Its principal axis should be oriented at 0 deg. The phase shifter can be placed anywhere in the optical path between the polarizer and the analyzer. One useful option is to integrate the phase shifter with one of the OI-DIC beam shearing assemblies, as shown in Fig. 1.

Two built OI-DIC assemblies replace standard DIC sliders in upright and inverted Olympus microscopes, BX and IX series (Olympus, Tokyo, Japan).²⁴ One assembly is located in the illuminating beam from the condenser side and another assembly is positioned in the imaging beam from the objective side. The phase shifter is included in one OI-DIC assembly only. Figure 2 shows a standard high-resolution Olympus DIC slider U-DICTHR (objective-side) and prism U-DIC40HR (condenser-side), and new sliders with the beam-shearing assemblies, OI-DIC-A (objective-side) and OI-DIC-B (condenser-side), in the transmitted white light. The prism U-DIC40HR is mounted in the DIC slider for an Olympus DICD condenser. There are two crossed polarizers at the entrance and exit of the beam. The DIC prisms and the beam-shearing assemblies split the input light into two output orthogonally polarized beams with

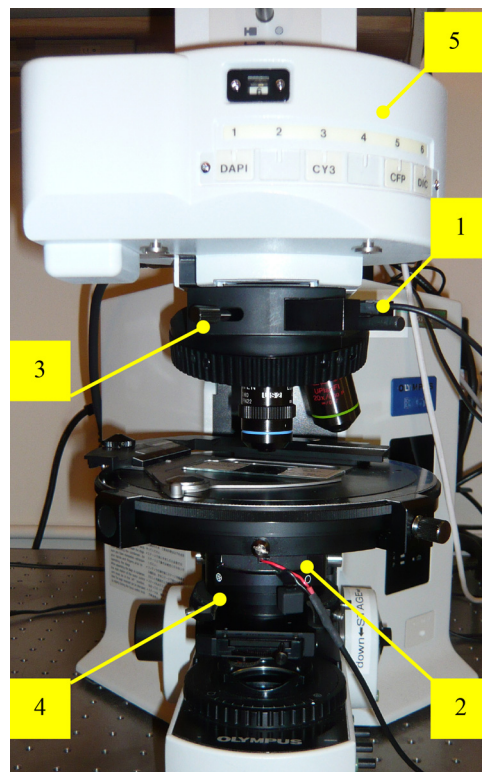


Fig. 3 Olympus upright microscope BX61 with OI-DIC. (1) Objective-side assembly OI-DIC-A; (2) condenser-side assembly OI-DIC-B; (3) revolving nosepiece U-P4RE; (4) condenser DICD; and (5) motorized fluorescence illuminator BX-RFAA with 6 cube turret.

a small shearing angle. The output beams generate interference fringes, which are perpendicular to the shear plane. The top row shows that the shear plane of the Olympus DIC prisms is oriented at 0 deg. The shear plane of the OI-DIC beam-shearing assemblies is oriented at -45 deg in the OFF state (central row) and at $+45$ deg in the ON state (bottom). The distance between the interference fringes is inversely proportional to the shear angle. Therefore, interference fringes in the assembly OI-DIC-A are located about 1.5 times closer to each other in comparison to the Olympus DIC slider U-DICTHR. Because of small shear angles, Olympus DIC prism U-DIC40HR and condenser-side assembly OI-DIC-B display a single interference fringe that appears alone because the fringe period is greater than the width of the aperture.

Figure 3 shows an example of the OI-DIC set-up based on the microscope Olympus BX61. The objective-side slider OI-DIC-A is inserted into the position provided on the revolving nosepiece U-P4RE. The condenser-side slider OI-DIC-B is placed into the position provided on the condenser DICD. The condenser contains a rotatable linear polarizer and quarter-wave plate, which both form the Senarmont compensator. The compensator allows us to adjust an initial bias between the interfering beams.

We use the Cartesian X - Y coordinates for description of component orientations in the optical pathway. The X -axis is parallel to the observer (East-West), and the Y -axis is away from the observer (North-South). The slot in the nosepiece for the objective-side DIC slider is oriented at a 45 -deg angle (northwest to southeast). Therefore, the OI-DIC assemblies introduce a shear, which is parallel or perpendicular to the X -axis (East-West or

North-South). The standard DIC prisms create a shear in direction from northwest to southeast.

The DIC mirror unit U-MDICT, which serves as an analyzer, is mounted on the turret of the motorized fluorescence illuminator BX-RFAA. This setup can be used for imaging the specimen under investigation with OI-DIC and reflected fluorescence techniques. In order to switch between OI-DIC and fluorescence, the motorized illuminator moves either the DIC mirror unit or the fluorescence mirror cube in the light path.

3 Mapping the Optical Path Length Gradient Vector

For simplicity of description, let us consider a phase nonbirefringent specimen with two-dimensional (2-D) distribution of OPL $\phi(x, y)$. Then the OPL gradient vector $\mathbf{G}(x, y) = \nabla\phi(x, y)$ is the following:

$$\begin{aligned} G(x, y) &= \left[\frac{\partial\phi(x, y)}{\partial x}, \frac{\partial\phi(x, y)}{\partial y} \right] \\ &= [\gamma(x, y) \cos \theta(x, y), \gamma(x, y) \sin \theta(x, y)], \end{aligned} \quad (1)$$

where $\gamma(x, y)$ is the gradient magnitude and $\theta(x, y)$ is the gradient azimuth. We would like to mention that the gradient magnitude represents an increment of the OPL, which is in nanometers, along the lateral coordinate, which is also in nanometers. Thus, the gradient magnitude is unitless.

The intensity distribution in the DIC image $I(x, y)$ can be described by using a model of interference of two overlapping identical coherent images, slightly offset from each other along the X - or Y -axis by the shear distance $\sqrt{2}d$ and shifted by bias Γ ⁸

$$\begin{cases} I_1(x, y) = \tilde{I}(x, y) \sin^2 \left(\frac{\pi}{\lambda} \left\{ \Gamma + \sqrt{2}d \cdot \gamma(x, y) \cos[\theta(x, y)] \right\} \right) + I_c(x, y) \\ I_2(x, y) = \tilde{I}(x, y) \sin^2 \left(\frac{\pi}{\lambda} \left\{ \Gamma + \sqrt{2}d \cdot \gamma(x, y) \sin[\theta(x, y)] \right\} \right) + I_c(x, y) \end{cases}, \quad (2)$$

where $\tilde{I}(x, y)$ and λ are intensity and wavelength of the illuminating beam, and $I_c(x, y)$ is the stray light intensity. Image intensities $I_1(x, y)$ and $I_2(x, y)$ correspond to the X shear direction (OFF state) and the Y shear direction (ON state). Equation (2) takes into account that the combined shear distance between two interfering beams in the OI-DIC equals the shear distance produced by a single DIC prism d multiplied by $\sqrt{2}$. Earlier, Shribak described two simple methods for determining the shear angle by measuring the retardance variation of a single DIC prism in the transmitted or in the reflected light and tabulating the shear distance produced by standard Olympus DIC prisms with various objective lenses.^{6,7} The shear distance is a product of the focal distance of the objective lens and the shear angle of the DIC prism.

In order to find the OPL gradient vector $\mathbf{G}(x, y)$ with magnitude $\gamma(x, y)$ and azimuth $\theta(x, y)$, we capture and process several DIC images with different biases and shear directions.

The optimal approach to computation of the gradient vector map depends on the specimen under investigation and the shear distance between two interfering beams, which in its turn is determined by the type of the DIC prisms and the focal distance of the objective lens. High-resolution DIC prisms and high magnification objective lenses produce the smallest shear amount, while high-contrast DIC prisms and low magnification objective lenses create the largest shear distance. The highest contrast in DIC imaging occurs when bias equals the optical path difference introduced by the specimen ($\Gamma \approx \sqrt{2}d\gamma$).^{6,7} Then bias compensation is adjusted to

extinguish the light coming from one edge of the object of interest. This result agrees with data obtained by Salmon and Tran.²⁵ They found that for the edges of organelles and cells, the optical path difference corresponds to about $1/10$ th the wavelength or greater, but for microtubules and tiny organelles in a cell, the optical path difference is very small, less than $1/100$ th the wavelength of green light. Salmon and Tran recommend using about $1/15$ th to $1/20$ th the wavelength bias for observation of microtubules in order to have sufficient light at the camera. A similar result was found by Schnapp.²⁶ Alternatively Allen and others suggested a bias $1/9$ th to $1/4$ th the wavelength for imaging human buccal epithelial cells and *Allogromia*.²⁷ They also mentioned that a large bias is less sensitive to polarization aberrations and allows reduction of the exposure time. Unfortunately, neither Salmon nor Allen specified the shear amount, which is an important parameter in the bias consideration.

We have developed two groups of algorithms for computing a map of the OPL gradient vector. The first group employs DIC images captured near extinction with a small adjustable bias.^{8,21} This approach provides high contrast of the weak specimen, as was suggested by Salmon and Tran.²⁵ However, DIC images near extinction require using either a high-brightness light source, such as arc lamp or longer exposure time. The high extinction factor is also required. These factors are especially important for high-resolution imaging when the shear distance is small. The first group includes algorithms using DIC images, which are captured with two orthogonal shear directions and

biases $\Gamma = -\Gamma_0; 0; \Gamma_0$ (2×3 -frame algorithm with extinction setting) and $\Gamma = -\Gamma_0; \Gamma_0$ (2×2 -frame algorithm without extinction setting). For visualization of fast moving organelles, it is possible to use only two specimen images with orthogonal shear directions and the same bias $\Gamma = \Gamma_0$ (two-frame algorithm with background subtraction). However, the two-frame algorithm can only be used when the specimen's absorption and scattering are negligible and the illuminating light is highly stable and uniform. The first group is similar to the early algorithms Shribak proposed for quantitative orientation-independent differential polarized light microscopy applied to mapping 2-D birefringence distribution in a specimen with low retardance.^{28,29}

The second group of algorithms employs two orthogonal shear directions and a set of biases, which are evenly distributed over one wavelength region. Recently, Shribak presented the algorithm for mapping the OPL gradient vector using a quarter-wave step in the bias, $\Gamma = 0; \lambda/4; \lambda/2; 3\lambda/4$ (2×4 -frame algorithm with $\lambda/4$ bias step).⁷ A comparable 2×4 -frame algorithm was described by Arnison et al.¹¹ for phase imaging using a DIC microscope with the rotated specimen. The second group

is similar to the phase-shifting algorithms commonly used in interferometry.³⁰

Which algorithm group is used depends on the OPL gradient range of the specimen. The first algorithm group is more suitable for specimens with low OPL gradients. The second algorithm group does not require the user to estimate the optical path difference range in advance, such as when a large optical path difference is present. Also, the second group requires a lower beam intensity and lower extinction. The researcher could start with an algorithm from the second group in order to estimate the specimen's optical path difference and then apply an algorithm from the first group with the optimized bias amount.

For the convenience of the reader and for consistency with the further explanation, we will briefly outline the 2×3 -frame algorithm with extinction setting and small adjustable bias. The algorithm was initially proposed for the OI-DIC with rotatable stage and single DIC prisms in the illumination and imaging paths.⁸ Currently, we apply this algorithm in most experiments. The typical bias used Γ_0 is 0.15λ . Six DIC images for the 2×3 -frame algorithm with extinction setting are described by the following equation system, which is derived from Eq. (2):

$$\begin{cases} I_{1j}(x, y) = \tilde{I}(x, y) \sin^2 \left(\frac{\pi}{\lambda} \left\{ j\Gamma_0 + \sqrt{2}d \cdot \gamma(x, y) \cos[\theta(x, y)] \right\} \right) + I_c(x, y) \\ I_{2j}(x, y) = \tilde{I}(x, y) \sin^2 \left(\frac{\pi}{\lambda} \left\{ j\Gamma_0 + \sqrt{2}d \cdot \gamma(x, y) \sin[\theta(x, y)] \right\} \right) + I_c(x, y), \end{cases} \quad (3)$$

where $j = -1, 0, 1$.

Initially, two terms are computed

$$\begin{cases} A_1(x, y) = \frac{I_{1,1}(x, y) - I_{1,-1}(x, y)}{I_{1,1}(x, y) + I_{1,-1}(x, y) - 2I_{1,0}(x, y)} \tan \left(\frac{\pi\Gamma_0}{\lambda} \right) = \tan \left\{ \frac{2\sqrt{2}\pi}{\lambda} d\gamma(x, y) \cos[\theta(x, y)] \right\} \\ A_2(x, y) = \frac{I_{2,1}(x, y) - I_{2,-1}(x, y)}{I_{2,1}(x, y) + I_{2,-1}(x, y) - 2I_{2,0}(x, y)} \tan \left(\frac{\pi\Gamma_0}{\lambda} \right) = \tan \left\{ \frac{2\sqrt{2}\pi}{\lambda} d\gamma(x, y) \sin[\theta(x, y)] \right\}. \end{cases} \quad (4)$$

Notice that the above ratios eliminate intensities of light that have interacted with the specimen. This operation suppresses contributions of absorption and scattering if they do not modify a beam polarization. In the case of imaging a sample with birefringence or dichroism, the mathematical model becomes significantly more complex and Eqs. (2)–(4) have to be corrected. We do not consider birefringent and dichroic specimens in the current article.

Then we calculate magnitude $\gamma(x, y)$ and azimuth $\theta(x, y)$ of the OPL gradient vector $\mathbf{G}(x, y)$:

$$\begin{cases} \gamma(x, y) = \frac{\lambda}{2\sqrt{2}\pi d} \sqrt{\arctan^2[A_1(x, y)] + \arctan^2[A_2(x, y)]} \\ \theta(x, y) = \arctan \left[\frac{\arctan A_2(x, y)}{\arctan A_1(x, y)} \right]. \end{cases} \quad (5)$$

The shear distance d can be measured as described in our previous publications.^{6,7}

We would like to introduce a 2×3 -frame algorithm with a third-wave step in the bias, $\Gamma = -\lambda/3; 0; \lambda/3$. This algorithm represents the second group, and it is similar to the three-frame algorithm, which is used in optical interferometry.³¹

In this case, Eq. (2) can be rewritten

$$\begin{cases} I_{1j}(x, y) = \tilde{I}(x, y) \sin^2 \left\{ \frac{\pi}{3} j + \frac{\sqrt{2}\pi d}{\lambda} \cdot \gamma(x, y) \cos[\theta(x, y)] \right\} + I_c(x, y) \\ I_{2j}(x, y) = \tilde{I}(x, y) \sin^2 \left\{ \frac{\pi}{3} j + \frac{\sqrt{2}\pi d}{\lambda} \cdot \gamma(x, y) \sin[\theta(x, y)] \right\} + I_c(x, y), \end{cases} \quad (6)$$

where $j = -1, 0, 1$.

Then two terms are computed

$$\begin{cases} \tilde{A}_1(x, y) = \frac{[I_{1,1}(x, y) - I_{1,-1}(x, y)]\sqrt{3}}{I_{1,1}(x, y) + I_{1,-1}(x, y) - 2I_{1,0}(x, y)} = \tan \left\{ \frac{2\sqrt{2}\pi}{\lambda} d\gamma(x, y) \cos[\theta(x, y)] \right\} \\ \tilde{A}_2(x, y) = \frac{[I_{2,1}(x, y) - I_{2,-1}(x, y)]\sqrt{3}}{I_{2,1}(x, y) + I_{2,-1}(x, y) - 2I_{2,0}(x, y)} = \tan \left\{ \frac{2\sqrt{2}\pi}{\lambda} d\gamma(x, y) \sin[\theta(x, y)] \right\}. \end{cases} \quad (7)$$

Equation (7) can be easily derived from Eq. (4) by substituting $\sqrt{3}$ instead of $\tan(\pi\Gamma_0/\lambda)$.

Finally, we obtain the 2-D distribution of magnitude $\gamma(x, y)$ and azimuth $\theta(x, y)$ of the OPL gradient vector $\mathbf{G}(x, y)$

$$\begin{cases} \gamma(x, y) = \frac{\lambda}{2\sqrt{2}\pi d} \sqrt{\arctan^2[\tilde{A}_1(x, y)] + \arctan^2[\tilde{A}_2(x, y)]} \\ \theta(x, y) = \arctan \left[\frac{\arctan \tilde{A}_2(x, y)}{\arctan \tilde{A}_1(x, y)} \right]. \end{cases} \quad (8)$$

The new 2×3 -frame algorithm is faster than the previously reported 2×4 -frame algorithm.⁷ It is more suitable for use by a potential real-time OI-DIC while simultaneously capturing multiple images. It is also possible to adapt other algorithms, which are used in phase-shifting interferometry,³² for computing the OPL gradient vector.

The obtained OPL gradient vector map also includes some contribution from wavefront aberrations introduced by the microscope optics, glass slide or dish, coverslip, and so on. This contribution can be removed by the background correction procedure, which Shribak described earlier.⁷

4 Mapping the Optical Path Length

The obtained 2-D distribution of the OPL gradient vector $\mathbf{G}(x, y)$ can be used for computing the OPL map. The reconstruction of a parameter from its gradient fields is a classical problem (the Poisson equation) common in many areas of research including computer vision. Our initial approach was to integrate the OPL gradient image in each direction of shear.^{8,11} However, the numerical integration has drawbacks such as a directional streaking effect. Because an OPL gradient vector represents a conservative vector field, the computed OPL depends only on the endpoints of that integral, not the particular integration route taken. Therefore, integration along multiple routes can reduce the directional artifacts.

Currently, for computing of OPL maps, we employ the technique based on Fourier integration. The 2-D OPL gradient vector $\mathbf{G}(x, y)$ [Eq. (1)] can be presented as a complex number

$$\mathbf{G}(x, y) = \frac{\partial \phi(x, y)}{\partial x} + i \frac{\partial \phi(x, y)}{\partial y} = \gamma(x, y) e^{i\theta(x, y)}, \quad (9)$$

where the real and imaginary parts are the X - and Y -components of the OPL gradient vector, respectively.

At first we apply the 2-D Fourier transform to the left and the middle parts of the equation above. Then the resultant integral equation can be solved by partial integration. After using the inverse 2-D Fourier transform, we receive the following equation for computation of the OPL $\phi(x, y)$:

$$\phi(x, y) = F^{-1} \left\{ \frac{F[\mathbf{G}(x, y)]}{i(\omega_x + i\omega_y)} \right\}, \quad (10)$$

where ω_x and ω_y are spatial angular frequencies.

Taking into account the right part of Eq. (10), we finally get

$$\phi(x, y) = F^{-1} \left\{ \frac{F[\gamma(x, y) e^{i\theta(x, y)}]}{i(\omega_x + i\omega_y)} \right\}. \quad (11)$$

The Fourier solution of the Poisson equation is obtained above from the magnitude $\gamma(x, y)$ and azimuth $\theta(x, y)$ of the OPL

gradient vector. This approach is similar to the spiral phase method described by Arnison et al.¹¹ In our case, a calibration is unnecessary, as demonstrated by the result shown in Fig. 5.

In principle, the OPL can be also computed by using subtraction terms $I_{1,1}(x, y) - I_{1,-1}(x, y)$ and $I_{2,1}(x, y) - I_{2,-1}(x, y)$, which allows faster processing [see Eq. (4)]. But the obtained data have to be corrected to take into account the shear distance, nonuniformity of illumination, specimen absorption and scattering, and the beam depolarization. Because the shear distance is less than the optical resolution, the subtraction method and gradient methods give equivalent results when the optical blur and noise considerations are added. Therefore, the results should not be different in any meaningful way for subtraction versus gradient.

5 Enhanced OPL Map Computation Using Deconvolution

The OPL method described in the previous section corrects for the differential nature of the DIC map formation process. However, the resolution of the map can be further enhanced by applying a deconvolution algorithm to correct for the optical imaging limitations of the microscope. The DIC images normally have a high signal-to-noise ratio (SNR), which allows for the effective use of linear filters such as the Wiener filter, rather than the more complex and nonlinear iterative deconvolution algorithms that are better suited to low light fluorescence imaging applications. Low light fluorescence has Poisson distributed noise and typically bright features on a dark background. This leads to iterative ML methods such as the Richardson Lucy technique. The OPL data have very different image characteristics, with bright and dark features on a gray background. The images are also not light limited and have a high SNR with Gaussian distributed noise. In this case, the RL iterations and the Wiener method give almost identical results. Therefore, we can save processing time and other complications by using the single-step Wiener filtering approach.

The Wiener filter of the OPL map can be described in the Fourier domain as follows

$$\phi_{\text{WF}}(x, y) = F^{-1} \left\{ F[\phi(x, y)] \cdot \frac{H^*(x, y)}{|H(x, y)|^2 + k} \right\}, \quad (12)$$

where $H(x, y)$ is the Fourier transform of the 2-D point-spread function (PSF) of the microscope objective lens, which can be calculated from the optical imaging parameters. The PSF refers to the intensity PSF of the optical path when the DIC components are excluded, since the DIC correction is handled separately. $H^*(x, y)$ is the complex conjugate of $H(x, y)$. The regularization parameter, k , is used to control the tradeoff between resolution enhancement and noise amplification, and a typical value is 10^{-6} . The integrated intensity of the PSF is unity, so the Wiener filter does not change the total intensity of the OPL map. Additionally, while the Wiener filter can generate negative values with respect to the background level, this is valid in an OPL image where the integrated phase can be negative. The OPL map intensity describes the total OPL difference with respect to the background at each point in the specimen. The optical limitations described by the PSF cause the OPL features to be less well defined and spread out; however, the total OPL is conserved. In the same way that fluorescence imaging has a conservation of total photons, the Wiener filter conserves

the total OPL over the map. OPL can be equated to the dry mass of a specimen.

The Wiener filter can be precalculated and efficiently applied as part of the OPL calculation in Eq. (11), such that no additional Fourier transform operations are required. The approximations are that the amplitude components are removed by calculating the background of the image with no DIC shear. The differential phase components are converted to OPL values, which are assumed to be incoherent.

The deconvolution algorithm on its own does not produce a phase image or OPL map. The deconvolution enhances the resolution/contrast of the image without changing the quantitative accuracy. In fact, it improves the accuracy of closely spaced structures. The deconvolution attempts to correct for the loss of resolution/contrast due to the optical limitations of the instrument and is applied to the OPL map. The OPL map has already been calculated from the DIC images, thus the deconvolution does not affect the accuracy of the OPL calculation. The deconvolution is only applied to the 2-D slices and not the 3-D volume, and thus only improves the lateral resolution. The high NA objective results in fine optical sectioning, so the images are treated as 2-D. The 2-D method presented shows significant contrast and resolution enhancement. Moving to full 3-D processing is the next step. We plan to measure a subresolution glass bead and compare the PSF to a theoretical model. Then we will apply the deconvolution to the 3-D volume.

6 Enhanced OPL Image Computation Using the Inverse Riesz Transform

In some situations, the exact linear (quantitative) mapping of OPL to image grayscale is not essential, and a more visually informative (qualitative) rendering is desired. There is a simple method to combine the two orthogonal differential images in a way that maintains the strong edge emphasis, yet enforces isotropy (that is to say rotation invariance). The method has been called the inverse Riesz transform and is actually equivalent to the sum of a pair of 2-D linear filters separately operating on the two differential images. However, the spatial exposition is rather complicated and belies the simplicity of the Fourier domain analysis.

The Riesz transform is a way to factorize the (linear) spatial gradient operator into a composition of two (linear) spatial operators. One is the (isotropic) square root of the negative Laplacian operator. The other is a pair of highly directional Riesz transforms. The idea, then, in image visualization, is to partially undo the gradient operator using the inverse Riesz transform pair. This then just leaves the square root Laplacian, which is simply equivalent to an isotropic high pass filter. The mathematical formulation is straightforward using the complex formulas of Sec. 4, i.e., Eqs. (10) and (11). If we denote the inverse Riesz transform of the gradient by $\rho(x, y)$, then:

$$\begin{aligned} \rho(x, y) &= F^{-1} \left\{ F[\gamma(x, y)e^{i\theta(x, y)}] \frac{|\omega_x + i\omega_y|}{i(\omega_x + i\omega_y)} \right\} \\ &= F^{-1} \left\{ F[\gamma(x, y)e^{i\theta(x, y)}] \frac{(\omega_x - i\omega_y)}{i\sqrt{\omega_x^2 + \omega_y^2}} \right\}. \end{aligned} \quad (13)$$

In fact, the Riesz multiplier in the right-hand side of Eq. (13) can actually be written simply as a unit magnitude Fourier phase spiral whose complex conjugate is equal to its inverse

$$\begin{aligned} e^{i\psi(\omega_x, \omega_y)} &= \frac{\omega_x + i\omega_y}{\sqrt{\omega_x^2 + \omega_y^2}}, \\ \frac{1}{e^{i\psi(\omega_x, \omega_y)}} &= e^{-i\psi(\omega_x, \omega_y)} \frac{\omega_x - i\omega_y}{\sqrt{\omega_x^2 + \omega_y^2}}. \end{aligned} \quad (14)$$

The inverse Riesz transform can then be written compactly as a negative spiral phase multiplication sandwiched between a forward and inverse Fourier transform

$$\rho(x, y) = F^{-1} \{ e^{-i\psi(\omega_x, \omega_y)} F[\gamma(x, y)e^{i\theta(x, y)}] \}. \quad (15)$$

Spiral phase Fourier operators were first proposed for interferometric image processing by Larkin.³³ More details of the above method for isotropically combining differential images, such as x-ray phase images, can be found in the work of Larkin.³⁴ A one-dimensional analog using Hilbert transforms works in a similar fashion.³⁵

Note that the quantitative spiral phase method of Arnison¹¹ requires an additional boundary condition to get an accurate reconstruction. The simple Fourier method ignores boundary conditions and implicitly applies periodic conditions. The inverse Riesz spiral phase method also ignores boundary conditions, but the resultant errors are usually barely visible. Note that both complex spiral phase methods can yield imaginary as well as real component images. The imaginary component is related to a discrepancy or failure of the two differential images to satisfy the gradient relation. In effect, the (imaginary) discrepancy measures the curl component of a vector (two components) field, while the real part measures the gradient component. The splitting into real and imaginary components is equivalent to the Helmholtz–Hodge decomposition of classical vector analysis.

Differential image processing using Eq. (15) is a highly stable unitary operation because the spiral phase multiplier has unit magnitude. The well-known instability in the solution of the Poisson equation is avoided by replacing the division operator with a unitary multiplier. Examples of the inverse Riesz transform applied to DIC images are shown in Secs. 7 and 8.

The inverse Riesz transform image can be considered to be an OPL image that has been edge enhanced. The enhancement is equivalent to a high-pass or “sharpen” image processing filter. Although it is equivalent, it actually computes the result directly and avoids the full OPL computation as an intermediate step.

7 OI-DIC Flow-Chart

The OI-DIC processing is illustrated by the flowchart shown in Fig. 4. The figure displays images of diatom *Arachnoidiscus*, which is an excellent specimen for demonstrating advantages of the OI-DIC technique. It has a silicified cell wall, which forms a radially symmetric pillbox-like shell (frustule) composed of overlapping halves that contain intricate and delicate patterns. Sometimes it is called “a wheel of glass.” Diatom *Arachnoidiscus* deserves the term of “living photonic crystals” and was employed for enabling subdiffractive focusing with better confining of the light beam than other far-field super focusing approaches.³⁶ Birefringence of the *Arachnoidiscus* structure is very low, except for the central radial filaments that exhibit slightly elevated retardance. According to our previous measurement,²⁹ retardance of the central filaments is about 5 nm.

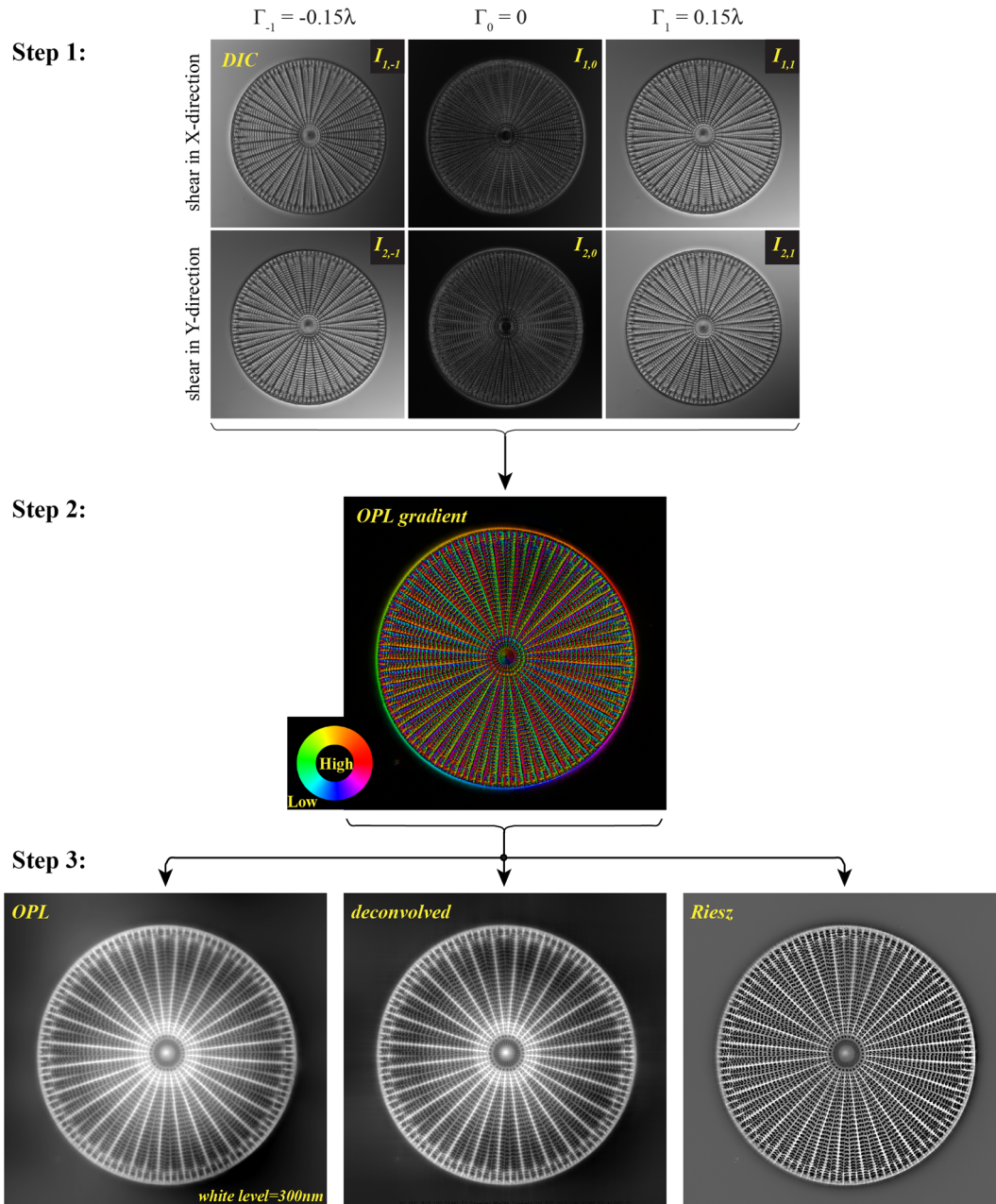


Fig. 4 OI-DIC flow-chart.

We used the objective lens Olympus UPlanFL 40 \times /0.75 P, projection lens (video camera adapter) Olympus U-TV0.5XC-3, and CCD camera Lumenera Infinity 3-1M. The camera chip has 1392 \times 1040 pixels with pitch 6.45 \times 6.45 μm^2 . The microscope Olympus BX61 was equipped with a 100 W halogen lamp and bandpass filter with the central wavelength $\lambda = 546 \text{ nm}$ and bandwidth 10 nm. The combined shear distance was 254 nm.⁷

At step 1 we captured a set of 2 \times 3 DIC images with X- and Y-shear directions and biases $\pm 0.15\lambda$ and 0. Image size is 345 $\mu\text{m} \times$ 335 μm . The total acquisition time was $\sim 1 \text{ s}$. The limiting factor of temporal resolution in the current OI-DIC microscope is the slow response time of the LC components. The temporal resolution also depends on the intensity of the illuminating beam. In the case of imaging a living sample, the

beam's maximum intensity is restricted in order to avoid sample damage. Instead of increasing the beam's intensity, we can use pixel binning. But pixel binning reduces the spatial resolution. Using ferro-electric LC cells instead of TN cells, and a mercury arc lamp instead of a halogen light source should allow us to achieve a total acquisition time of $\sim 0.2 \text{ s}$.

At step 2, the captured image set is processed according to Eqs. (4) and (5) in order to obtain the OPL gradient map. The middle image displays this map in pseudocolor. Here the gradient magnitude is linearly proportional to the image brightness, where the white level is 0.5 nm/nm. The gradient azimuth is represented by hue, as the color wheel in the left bottom corner illustrates.

At step 3, the gradient map is converted to the OPL map by the inverse Fourier transform, as shown in Eq. (10). The left

bottom image displays the OPL map of diatom *Arachnoidiscus*, where the OPL is linearly proportional to the image brightness with a white level of 300 nm. The OPL gradient map is also used for computing enhanced images. The deconvolved image with suppressed out-of-focus contribution is shown in the middle. The right picture was obtained with the inverse Riesz transform, which enhanced small details (high spatial frequencies).

8 Experimental Verification

To experimentally verify resolution of the OI-DIC technique, we employed microscope Olympus BX-61 (Olympus America Inc., Center Valley, Pennsylvania) equipped with two beam shearing assemblies, as shown in Fig. 3. We used a UPlanFL 100 \times /1.30 Oil P objective lens (Olympus); narrow-bandpass interference filter (546 nm, 10-nm FWHM; Chroma Technology, Rockingham, Vermont); and monochromatic CCD camera Infinity 3-1M with pixel pitch 6.45 \times 6.45 μm^2 (Lumenera, Ottawa, Canada). The top beam shearing assembly utilized two high-resolution Nomarski prisms U-DICTHR (Olympus), which create a combined shear distance of 100 nm.⁷ We accomplished image acquisition and analysis using MATLAB[®] (the MathWorks Inc., Natick, Massachusetts), which was enhanced by custom software functions.

8.1 Mapping OPL of Glass Rods in Liquids with the Different Refractive Indices

At first we explored a model specimen, which is optically similar to transparent filaments in living organisms. We took short segments of 4.1- μm -thick glass rods, which are used as spacers in LC cells, and embedded them in Cargille Certified Refractive Index Liquid (Cargille Labs, Cedar Grove, New Jersey).³⁷ The refractive index of the glass rod is 1.56. It was measured by matching to the corresponding refractive index liquid at wavelength 546 nm.

An example of the OPL map, which was computed with using the 2 \times 3-frame algorithm [Eqs. (3)–(5)] and Fourier integration [Eq. (11)], is shown in Fig. 5(a). The glass rod is embedded in immersion liquid with a refractive index of

1.51. The image brightness is linearly proportional to OPL, where the white level corresponds to 255 nm.

Figure 5(b) shows the cross-sections A-A' of the OPL maps of glass rods in immersion liquids with refractive indices of 1.47 (red curve), 1.51 (orange curve), 1.54 (blue curve), 1.56 (violet curve), and 1.58 (green curve). The extremum OPL is determined as

$$\text{OPL}_{\text{max}} = (n_r - n_l)t, \quad (16)$$

where n_r and n_l are the refractive indices of the rod and liquid, respectively, and t is the diameter of the rod. As one can see, the experimental OPL maxima and minimum 363 nm ($n_l = 1.47$), 205 nm ($n_l = 1.51$), 78 nm ($n_l = 1.54$), 0 nm ($n_l = 1.56$), and -84 nm ($n_l = 1.58$) are practically equal to the theoretical values 369 nm ($n_l = 1.47$), 205 nm ($n_l = 1.51$), 82 nm ($n_l = 1.54$), 0 nm ($n_l = 1.56$), and -82 nm ($n_l = 1.58$).

Figure 5(c) shows how OPL depends on the defocusing of the objective lens. When a microscope's objective is focused in middle of the rod ($z = 0 \mu\text{m}$), the experimental OPL (dotted red curve) fits the theoretical OPL (wide grey curve) precisely, except in small areas near the edges. The theoretical OPL is equal to the rod thickness profile multiplied by 0.05, which is the difference between the refractive indices of the rod and the liquid. The maximum OPL drops by about 5% when the specimen plane is located at the top (toward objective) or at the bottom (opposite to objective) of the rod's surface (blue and green dashed curves, correspondently). The OPL profile at the top is narrower when the microscope's objective is focused on the top surface. But when the specimen plane is moving farther away from the rod, the OPL is defocused more quickly toward the objective, as depicted by violet and orange dashed curves. In these cases, the specimen plane is placed at one-diameter distance from the top and the bottom of the rod, $z = -6 \mu\text{m}$ and $z = 6 \mu\text{m}$. Interestingly, above the rod, the maximum OPL decreases by 50%. The OPL diminishes by about 20% below the rod. This difference occurs because the rod works as a cylindrical lens.

The OPL noise level was about 0.5 nm. This level of sensitivity is similar to that reported by others developing

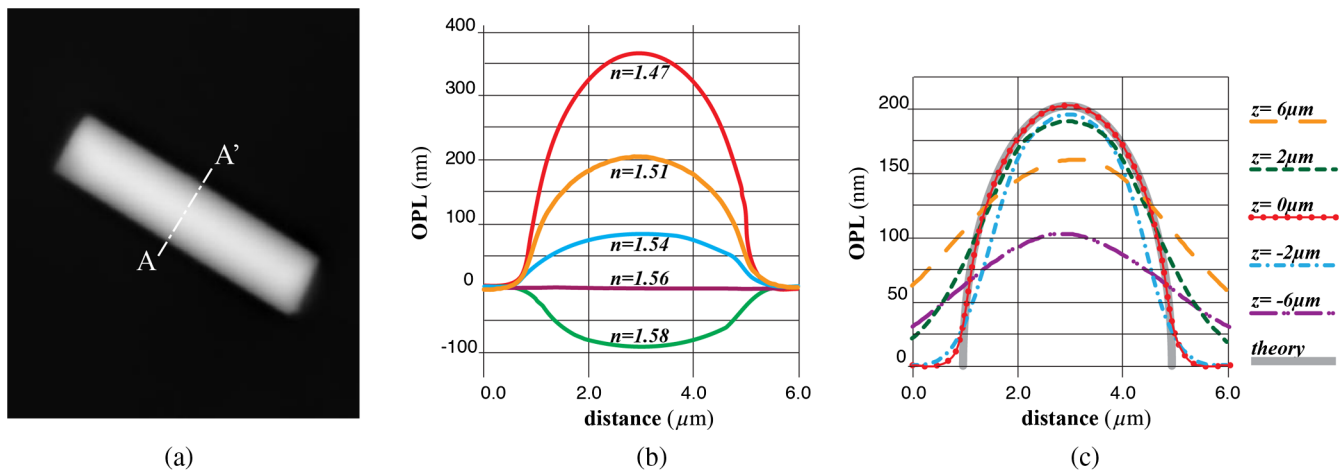


Fig. 5 (a) Computed grayscale OPL map of 4.1- μm -diameter glass rod embedded in liquid with refractive index 1.51; (b) cross-sections of the OPL maps of 4.1- μm -diameter glass rods in immersion liquids with the different refractive indices. The microscope's objective is focused in middle of the rods; (c) cross-sections of the OPL map of 4.1- μm -diameter glass rods in liquid with refractive index 1.51 at different positions of the specimen plane.

quantitative phase imaging methods. For example, the spatial light interference microscope (SLIM), which uses a phase contrast microscope and white light illumination, has an OPL sensitivity of 0.3 nm.³⁸ The sensitivity of the commercial version, called CellVista SLIM Pro, is <1 nm.³⁹ The 2 \times digital holographic microscope, developed by Cotte et al.,⁴⁰ demonstrated an OPL sensitivity of 2 nm.

8.2 Studying Lateral Resolution by Using Diatom *Frustulia rhomboides*

Diatom *Frustulia rhomboides* is an excellent specimen for testing the lateral resolution of the OI-DIC. Diatoms build their external skeleton (the valve) by catching silicate from the water and depositing it with amazing precision in specific pattern. A protective nanostructured shell has to be light enough to prevent sinking while simultaneously offering strength against predators. *F. rhomboides* has been popular with microscopists since Victorian times because it has been a standard test object to check the quality of their lenses. The interval between periodic striae (or lines) on *F. rhomboides* case is between 290 and 360 nm.⁴¹

Figure 6(a) shows an image of diatom *F. rhomboides* obtained with the deconvolution algorithm (Sec. 5). The cross-section A-A' of image brightness is shown in Fig. 6(b). The striae are clearly visible. The distance between striae is about 320 nm. The diameter of the Airy disk was 520 nm, which corresponds to a theoretical lateral resolution limit of 260 nm.⁴² The striae interval exceeds the resolution limit by only 20%, but the image contrast is about 35%, which is good. Other quantitative interference and phase microscopy techniques that use a restricted or modified condenser front focal plane aperture have lower lateral resolutions of the phase image. For example, the tomographic phase microscope developed by Habaza et al.⁴³ has a lateral resolution of 370 nm. The SLIM has a lateral resolution of 350 nm.^{38,39}

We think that using DIC prisms with smaller shear distance and correcting the wavefront aberrations will increase the lateral resolution. In particular, Noguchi et al.⁴⁴ demonstrated that the modulation transfer function (MTF) of a DIC microscope depends on the shear distance. The high-frequency region of

the MDF power spectrum increases if the shear distance decreases.

The resolution of the OI-DIC is also affected by wavefront aberrations. The PSF of an objective lens works as a “sharp knife” that “cuts” a thin optical section and creates an image of tiny organelles. If the specimen under investigation is thick, the PSF is blurred and works as a “dull knife.” The PSF can be corrected by using adaptive optics.

The method described here does not take into account the multiple scattering of light and assumes the object does not significantly scatter the illumination (according to the first-order Born approximation). Multiple scattering is one of the most challenging problems in optics, if we solved it completely, we could see through fog, murky water, or even human tissue. Recently, Kamilov et al. proposed the machine-learning tomographic approach to solve this problem.⁴⁵ The authors applied the machine-learning method for reconstructing the 3-D refractive index. Their experimental setup was based on a holographic optical-phase microscope equipped with galvanometric mirror that varies the angle of illumination of the sample. In principle, the OI-DIC microscope can be combined with the scanned aperture technique,⁴⁶ and it can provide initial data for the volumetric refractive index reconstruction based on the machine-learning approach.

8.3 Using the Inverse Riesz Transform for Imaging Thick Cells and Tissues

If the specimen under investigation has a thickness greater than 10 μm , then its subtle structures are often obscured by the out-of-focus images of larger components. The deconvolution procedure removes some out-of-focus contribution, but it can be not enough. In this case, the inverse Riesz transform, which enhances edges and small details, becomes very helpful.

Figure 7 shows a set of live images of the center of an unactivated surf clam *Spisula solidissima* oocyte, which was obtained using deconvolution and inverse Riesz transform algorithms. The set also shows a fluorescent image of chromosomes treated with Hoechst 33342 (DNA specific fluorescent marker). The pictures were taken using Olympus 30 \times /1.05 NA silicon oil objective lens UPLSAPO 30 \times S and photo eyepiece PE2.5 \times .

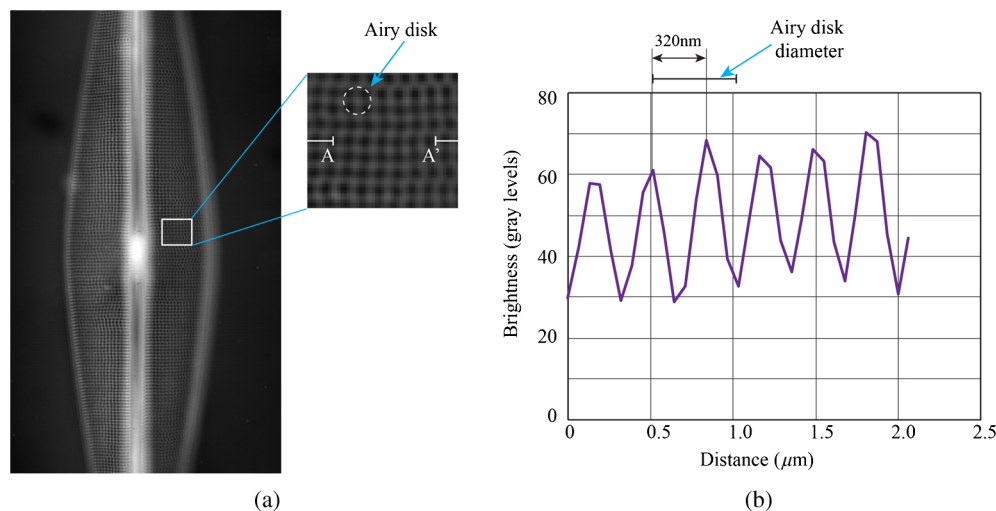


Fig. 6 (a) Image of diatom *F. rhomboides* computed with using deconvolution and (b) cross-sections A-A' of the image brightness.

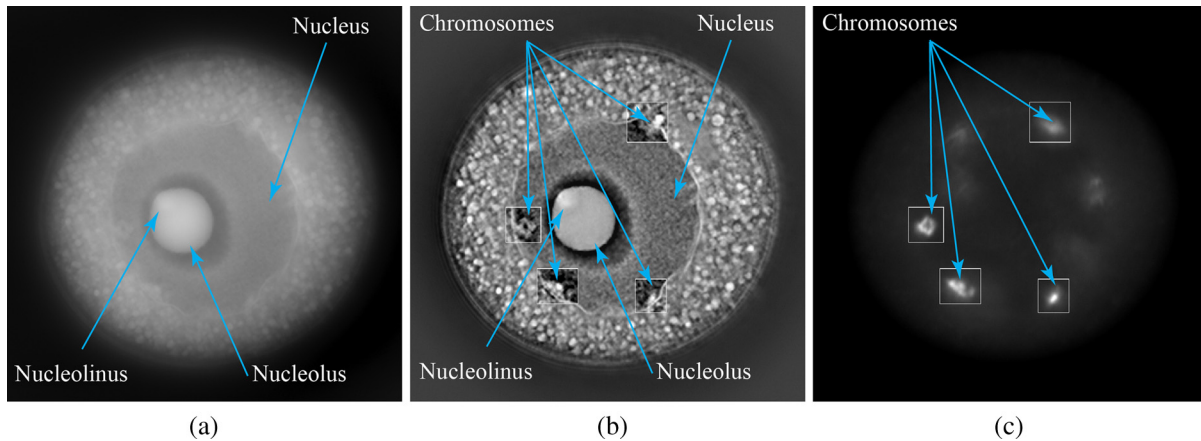


Fig. 7 Surf clam *S. solidissima* oocyte. (a) OI-DIC image obtained with deconvolution, (b) OI-DIC image obtained the inverse Riesz transform algorithms, and (c) fluorescent image with Hoechst 33342. Image size is $64 \mu\text{m} \times 64 \mu\text{m}$.

The diameter of the oocyte is $\sim 65 \mu\text{m}$. As one can see, the deconvolved image is quite blurry. The Riesz image depicts the nucleus envelope and granular nucleus structure clearly. The nucleolus boundary is sharp and the nucleolus is clearly visible. The nucleolus is an intranuclear organelle that has a role in regulating meiotic.⁴⁷ The diameter of nucleolus is $\sim 3 \mu\text{m}$ and the nucleolus is $\sim 10 \mu\text{m}$. The Riesz image also visualizes chromosomes with elevated concentrations of DNA. The Riesz and fluorescence images show four selected square areas with chromosomes.

9 Conclusion

Here we reported the quantitative OI-DIC microscope setup, which can easily replace standard DIC prisms in existing commercial microscope systems without modification. A new 2×3 -frame algorithm for computation of the OPL gradient map was introduced. We described computation of the OPL map using the obtained gradient vector map. We also described the deconvolution method for suppressing the out-of-focus contribution and the inverse Riesz transform technique for enhancing small details in the image. The reported experimental results confirm that the OI-DIC can achieve a lateral resolution of $\sim 300 \text{ nm}$ and an OPL noise level of 0.5 nm at a wavelength of 546 nm . Other interference and phase microscopy techniques use modified or restricted NAs of the condenser and/or objective lens. Therefore, their resolution is usually less than the resolution of regular brightfield imaging. They are also strongly affected by wavefront aberrations. Often times the contrast of raw images is low. The OI-DIC employs: (1) the full NAs of the condenser and objective lenses, (2) the optical image subtraction, and (3) the computation image subtraction. The OI-DIC also uses raw high-contrast images. Thus, the OI-DIC can provide the best resolution images.

Disclosures

The authors do not have conflicts of competing interest, financial or otherwise.

Acknowledgments

We thank Shinya Inoué of the Marine Biological Laboratory (Woods Hole, MA) for helpful discussion and Volodymyr Vasylyshyn (Lviv, Ukraine) for hardware development. This

publication was made possible by Grant No. R01-GM101701 from the National Institute of General Medical Sciences, National Institutes of Health. Its contents are solely the responsibility of the authors and do not necessarily represent the official views of the National Institute of General Medical Sciences or the National Institutes of Health.

References

1. F. H. Smith, "Interference microscope," U.S. Patent No. 2601175 (1947).
2. F. H. Smith, "Microscopic interferometry," *Research* **8**, 385–395 (1955).
3. G. Nomarski, "Interferential polarizing device for study of phase object," U.S. Patent No. 2924142 (1952).
4. R. D. Allen, G. B. David, and G. Nomarski, "The Zeiss-Nomarski differential equipment for transmitted-light microscopy," *Z. Wiss. Mikrosk. Mikrosk. Tech.* **69**(4), 193–221 (1969).
5. M. Pluta, *Advanced Light Microscopy. Vol. 2: Specialized methods*, Elsevier, Amsterdam, Netherlands (1989).
6. M. Shribak, "Differential interference contrast microscopy," in *Biomedical Optical Phase Microscopy and Nanoscopy*, N. T. Shaked, Z. Zalevsky, and L. L. Satterwhite, Eds., pp. 19–42, Elsevier, Oxford, United Kingdom (2012).
7. M. Shribak, "Quantitative orientation-independent DIC microscope with fast switching shear direction and bias modulation," *J. Opt. Soc. Am. A* **30**, 769–782 (2013).
8. M. Shribak and S. Inoué, "Orientation-independent differential interference contrast microscopy," *Appl. Opt.* **45**, 460–469 (2006).
9. C. Preza, "Rotational-diversity phase estimation from differential-interference-contrast microscopy images," *J. Opt. Soc. Am. A* **17**, 415–424 (2000).
10. C. Preza and J. A. O'Sullivan, "Implementation and evaluation of a penalized alternating minimization algorithm for computational DIC microscopy," *Proc. SPIE* **7533**, 75330E (2010).
11. M. R. Arison et al., "Linear phase imaging using differential interference contrast microscopy," *J. Microsc.* **214**(1), 7–12 (2004).
12. C. J. Cogswell et al., "Quantitative DIC microscopy using a geometric phase shifter," *Proc. SPIE* **2984**, 72–81 (1997).
13. S. V. King et al., "Calibration of a phase-shifting DIC microscope for quantitative phase imaging," *Proc. SPIE* **6443**, 64430M (2007).
14. S. V. King et al., "Quantitative phase microscopy through differential interference imaging," *J. Biomed. Opt.* **13**(2), 024020 (2008).
15. S. S. Kou and C. J. R. Sheppard, "Quantitative phase restoration in differential interference contrast (DIC) microscopy," *Proc. SPIE* **7000**, 700005 (2008).
16. B. Horn and M. J. Brooks, *Shape from Shading*, MIT Press, Cambridge, Massachusetts (1989).

17. T. J. McIntyre et al., "Differential interference contrast imaging using a spatial light modulator," *Opt. Lett.* **34**(19), 2988–2990 (2009).
18. T. J. McIntyre et al., "Quantitative SLM-based differential interference contrast imaging," *Opt. Exp.* **18**(13), 14063–14078 (2010).
19. R. N. Zahreddine et al., "Real-time quantitative differential interference contrast (DIC) microscopy implemented via novel liquid crystal prisms," *Proc. SPIE* **8227**, 822710 (2012).
20. C. C. Montarou and T. K. Gaylord, "Analysis and design of modified Wollaston prisms," *Appl. Opt.* **38**(31), 6604–6616 (1999).
21. M. Shribak, "Orientation-independent differential interference contrast microscopy technique and device," U.S. Patent No. 7233434 (2003).
22. M. Shribak et al., "Orientation-independent differential interference contrast (DIC) microscopy and its combination with orientation-independent polarization system," *J. Biomed. Opt.* **13**(1), 014011 (2008).
23. M. Shribak, "Orientation-independent differential interference contrast microscopy technique and device," U.S. Patent No. 7564618 (2003).
24. "Olympus microscopy. Research and clinical system solutions," <http://www.olympus-lifescience.com/en/> (23 December 2016).
25. E. D. Salmon and P. Tran, "High resolution video-enhanced differential-interference contrast (VE-DIC) light microscopy," *Methods Cell Biol.* **56**, 153–184 (1998).
26. B. J. Schnapp, "View single microtubules by video light microscopy," *Meth. Enzymol.* **134**, 561–573 (1986).
27. R. D. Allen, N. Strömberg Allen, and J. L. Travis, "Video-enhanced contrast, differential interference contrast (AVEC-DIC) microscopy: a new method capable of analyzing microtubule-related motility in the reticulopodial network of *allogromia laticollaris*," *Cell Motil.* **1**(3), 291–302 (1981).
28. M. Shribak and R. Oldenbourg, "Techniques for fast and sensitive measurements of two-dimensional birefringence distributions," *Appl. Opt.* **42**(16), 3009–3017 (2003).
29. M. Shribak, "Complete polarization state generator with one variable retarder and its application for fast and sensitive measuring of two-dimensional birefringence distribution," *J. Opt. Soc. Am. A* **28**(3), 410–419 (2011).
30. P. Hariharan, *Optical Interferometry*, 2nd ed., Academic Press, London, United Kingdom (2003).
31. P. Hariharan, B. F. Oreb, and N. Brown, "A digital phase-measurement system for real-time holographic interferometry," *Opt. Commun.* **41**(6), 393–396 (1982).
32. K. G. Larkin and B. F. Oreb, "Design and assessment of symmetrical phase-shifting algorithms," *J. Opt. Soc. Am. A* **9**(10), 1740–1748 (1992).
33. K. G. Larkin, D. Bone, and M. A. Oldfield, "Natural demodulation of two-dimensional fringe patterns: I. General background to the spiral phase quadrature transform," *J. Opt. Soc. Am. A* **18**, 1862–1870 (2001).
34. K. G. Larkin and P. A. Fletcher, "Isotropic scalar image visualization of vector differential image data using the inverse Riesz transform," *Biomed. Opt. Exp.* **5**, 907–920 (2014).
35. M. R. Arnison et al., "Using the Hilbert transform for 3D visualization of differential interference contrast microscope images," *J. Microsc.* **199**, 79–84 (2000).
36. E. De Tommasi et al., "Biologically enabled sub-diffractive focusing," *Opt. Exp.* **22**, 27214–27227 (2014).
37. "Cargille-Refractive Index Matching Liquids," <http://www.cargille.com/refractivestandards.shtml> (23 December 2016).
38. Z. Wang et al., "Spatial light interference microscopy (SLIM)," *Opt. Exp.* **19**, 1016–1026 (2011).
39. "Products-Phi Optics," <http://phioptics.com/products/> (23 December 2016).
40. Y. Cotte et al., "Marker-free phase nanoscopy," *Nat. Photonics* **7**, 113–117 (2013).
41. J. Vesela et al., "Ecological variation within traditional diatom morphospecies: diversity of *Frustulia rhomboides* sensu lato (Bacillariophyceae) in European freshwater habitats," *Phycologia* **51**(5), 552–561 (2012).
42. R. Oldenbourg and M. Shribak, "Microscopes," in *Handbook of Optics, Geometrical and Physical Optics, Polarized Light, Components and Instruments*, M. Bass, Ed., 3rd ed., Vol. I, pp. 28–281, McGraw-Hill, New York (2010).
43. M. Habaza et al., "Tomographic phase microscopy with 180° rotation of live cells in suspension by holographic optical tweezers," *Opt. Lett.* **40**, 1881–1884 (2015).
44. A. Noguchi et al., "Optical sectioning in differential interference contrast microscopy," *Opt. Commun.* **282**, 3223–3230 (2009).
45. U. S. Kamilov et al., "A learning approach to optical tomography," *Optica* **2**(6) 517–522 (2015).
46. M. Shribak and R. Oldenbourg, "Mapping polymer birefringence in three-dimensions using a polarization microscope with oblique illumination," *Proc. SPIE* **5462**, 57 (2004).
47. C. Chandsawangbhuwana et al., "High-throughput optofluidic system for the laser microsurgery of oocytes," *J. Biomed. Opt.* **17**(1), 015001 (2012).

Michael Shribak is from Novyi Rozdil, Lviv region, Ukraine. He graduated with a MSc in optics and spectroscopy from Lviv University in 1982 and a PhD in applied optics from Moscow University of Geodesy and Cartography in 1991. He has expertise in polarized light, optical microscopy, and digital imaging of living cells and microorganisms. He also has experience in fiber optics sensors and laser technology. He is now a scientist at Marine Biological Laboratory, Massachusetts.

Kieran G. Larkin originates from Kells, County Meath, Éire. He graduated with a BSc physics and MSc applied optics from Imperial College, London, in 1979 and 1981, then a PhD in physics from the University of Sydney in 2001. He has worked in optical and digital imaging since 1981, most notably with Crosfield Electronics, Rank Xerox, CSIRO, University of Sydney, and Canon research (CiSRA), where he was Distinguished Engineer. He is now an independent researcher.

David Biggs is originally from Auckland, New Zealand. He graduated with a BE (E&E) in 1994, and a PhD in 2000, both from the University of Auckland. He is expertise in image processing and the blind deconvolution of 2D and 3D images. He has worked extensively in the life science field working with datasets from fluorescence microscopes. He is now a consultant, researcher, and software developer living in Northern California.